International Journal of Mechanical Sciences 101-102 (2015) 214–226

Contents lists available at ScienceDirect

International Journal of Mechanical Sciences

journal homepage: www.elsevier.com/locate/ijmecsci

An efficient computational approach to evaluate the ratcheting performance of rail steels under cyclic rolling contact in service

Chung Lun Pun [a], Qianhua Kan [b], Peter J Mutton [c], Guozheng Kang [b], Wenyi Yan [a,*]

[a] Department of Mechanical and Aerospace Engineering, Monash University, Clayton VIC 3800, Australia
[b] Department of Applied Mechanics and Engineering, Southwest Jiaotong University, Chengdu 610031, People's Republic of China
[c] Institute of Railway Technology, Monash University, Clayton VIC 3800, Australia

ARTICLE INFO

Article history:
Received 23 April 2015
Received in revised form
4 August 2015
Accepted 7 August 2015
Available online 14 August 2015

Keywords:
High strength rail steel
Ratcheting performance
Finite element analysis
Cyclic rolling contact

ABSTRACT

A comprehensive study was carried out to numerically evaluate the ratcheting performance of three high strength pearlitic rail steels under different wheel–rail cyclic rolling contact conditions, i.e. free rolling, partial slip, and full slip conditions, different friction coefficients and different axle loads. The wheel–rail cyclic rolling contact was simulated by repeatedly passing a distributed contact pressure and a distributed tangential traction on the rail surface. This study combined the non-Hertzian contact pressure from finite element analysis with the longitudinal tangential traction from Carter's theory to simulate the wheel–rail cyclic rolling contact problems. A cyclic plasticity material model considering the non-proportionally loading effect developed recently by the authors was applied to simulate the ratcheting behaviour of rail steels. The ratcheting performance of the rail steels was evaluated by the crack initiation life which was determined from the stabilized ratcheting strain rate and the ductility limit of the rail materials. The numerical results indicate that the crack initiation life decreases with the increase of the normalized tangential traction, the friction coefficient and the axle load for all three rail steels. Among the three rail steels, the hypereutectoid rail steel grade with a lower carbon content provides the best ratcheting performance under higher axle loads such as those used railway transport of mineral products in Australia. Furthermore, the numerical results obtained in this study are in reasonable agreement with the in-service performance of the three rail steels. This indicates that the developed approach has the capacity to evaluate the ratcheting performance of other rail steels under service loading conditions. The outcomes can provide useful information to the development and application of rail steels and the development of effective rail maintenance strategies in order to mitigate rail degradation.

1. Introduction

In an actual wheel–rail rolling contact process, the rail is subjected to cyclic loading and the rail surface is subjected to rolling and sliding loading with high contact stresses. It has been found that the cyclic stresses and the plastic deformation are the major factors influencing the rail degradation processes [1,2]. The stresses endured by the rail are always multiaxial, non-proportional and randomly fluctuating in magnitude and direction [3]. If the wheel–rail cyclic rolling contact conditions result in a stress level above the plastic shakedown limit or ratcheting threshold, new plastic deformation will occur and accumulate, i.e. ratcheting occurs, under each loading cycle. Although the plastic deformation in the rail in each cycle may be very small, the plastic deformation accumulates to large values over many cycles of loading [4]. When the ratcheting strain reaches the limiting ductility of the rail, the rail will fail at the local material point, which corresponds to the initiation of wear or rolling contact fatigue [5–7], e.g., in the form of head checks in the rail head. This states that the ratcheting behaviour plays a key role in causing the rolling contact failure of the rail, i.e. wear and rolling contact fatigue damage. Additionally, the demanding conditions imposed by rail transport of mineral products with higher axle loads and increasing annual haulage rates give rise to rail degradation and the requirement for ongoing grinding to maintain operational safety of the rail. Selection of the most appropriate

* Corresponding author. Tel.: +61 3 990 20113; fax: +61 3 9905 1825.
E-mail address: wenyi.yan@monash.edu (W. Yan).

http://dx.doi.org/10.1016/j.ijmecsci.2015.08.008
0020-7403/

rail material grades becomes important, and for this reason, evaluation of the ratcheting performance of the available rail steel grade under service loading is necessary. Such information can be used to assess the consequences of changes to the service conditions, i.e. increasing axle load.

Due to the relatively high costs in conducting field tests, the finite element method has been widely applied to numerically simulate wheel–rail cyclic rolling contact problems [8–17]. Kulkarni et al. [8–10] conducted several numerical studies on the ratcheting behaviour in elastic–plastic with the kinematic-hardening, elastic-perfectly plastic materials, and actual rail material under cyclic frictionless pure rolling contact. A two-dimensional finite element model was also developed by Xu and Jiang [11] to simulate steady-state line rolling contact on a 1070 steel under partial slip conditions. Jiang et al. [12] generated a three-dimensional numerical model to investigate the partial slip conditions and the contact stresses under three-dimensional rolling contact. However, all these studies applied the Hertzian contact pressure distribution, which is originated from the Hertz contact theory [13] and is limited to elastic material properties and half-space assumptions. The study by Yan and Fischer [14] indicated that the assumptions employed in Hertz contact theory impose limitations of its applicability in wheel–rail rolling contact problems. Plastic deformation frequently takes place on both wheel and rail as the maximum contact pressure exceeds the elastic limit of both wheel and rail materials [15]. Some discrepancies in the contact pressure distribution between the analytical solutions and real situations may be found if the plastic deformation in contact zone is high [14–16]. These problems were also highlighted in the studies by Ringsberg [17] and his colleagues [18] who compared the numerical results obtained from Hertzian contact pressure and those obtained from non-Hertzian contact pressure. Their numerical results indicated that the use of non-Hertzian contact pressure in the finite element simulations can provide a more realistic simulation for wheel–rail cyclic rolling contact problems. Similar discussion was also given by Wen et al. [2]. According to this, a non-Hertzian contact pressure distribution, which was obtained from a separate three-dimensional wheel–rail contact simulation, was applied in current study.

Beside using accurate loading conditions, to accurately evaluate the ratcheting performance of rail steels under different service loading conditions in numerical studies, an appropriate cyclic plasticity material model, which can satisfactorily describe both uniaxial and multiaxial ratcheting behaviour of the rail materials, is of paramount importance for simulating wheel–rail cyclic rolling contact problems [19]. Although many cyclic plasticity constitutive models, i.e. Chaboche model [20–22] and Ohno–Wang model [23], for ratcheting simulation have been developed, it is still challenging to find a generic and precise constitutive model due to the complexity of ratcheting behaviour. For instance, some common models for nonlinear hardening cannot simultaneously simulate and predict ratcheting with acceptable accuracy [24]. Additionally, extensive studies of ratcheting have demonstrated that different materials exhibit different ratcheting behaviour and varying cyclic characteristics. This indicates that the existing models may not be reasonably and simultaneously capture the ratcheting behaviour of the rail materials, for instance, the isotropic softening behaviour of heat treated rail steels [25]. According to this, a cyclic plasticity material model, which was recently developed by the authors [25] based on the experimental results by coupling a non-proportional multi-axial parameter into isotropic softening and kinematic hardening rules, was applied to simulate the wheel–rail cyclic rolling contact problems in current study. The capability of this material model to simulate both uniaxial and biaxial ratcheting behaviour of the studied rail steels has been verified in [25]. Application of this material model can provide a more realistic quantification of plastic ratcheting in the rail head to evaluate the ratcheting performance of the rail steels under different loading conditions in service.

The performance of the rail steels can be evaluated based on the predicted crack initiation life of the rail steels under cyclic rolling contact conditions. In recent years, several models for rolling contact fatigue crack initiation have been developed, such as the equivalent strain approaches, energy-density based models and the empirical model [26]. One of the well-known models of the equivalent strain approaches is the Coffin–Manson relation, which is expressed in the total shear strain range, and the crack initiation life is determined based on the material plane with maximum total shear strain range [27]. However, it has been found that the equivalent strain approaches do not take into account the influence of multi-axial non-proportional loadings on the crack initiation life [28]. Another well-known model for rolling contact fatigue crack initiation is the energy-density based model, which was proposed by Smith et al. [29]. This model, which belongs to the strain-life phenomenological approach for multi-axial loading, takes into account mean stress effect and both elastic strain range and plastic strain range in multiaxial loading. Although it has been widely used for determining mode I fatigue crack initiation and growth, its application is mostly limited to tensile mean stresses, which cannot reflect the actual wheel/rail rolling contact situations. An empirical model proposed by Kapoor [5] has been applied to predict the fatigue crack initiation life due to ratcheting only. The crack initiation life from the empirical model is determined based on the equivalent ratcheting strain rate and the material ductility. Tyfour and Beynon [30] have found that ratcheting rather than low-cycle fatigue was the dominant damage mechanism under typical wheel/rail cyclic rolling contact conditions. Study from Kapoor [4] and Bandula-Heva and Dhanasekar [31] further confirmed that ratcheting plays a key role in causing rolling contact failure of rail steels. According to this, the empirical model was used to predict the crack initiation life for the purpose to evaluate the performance of the rail steels in the current study.

In this paper, three high strength pearlitic rail steels, a low alloy heat treated rail steel (LAHT) and two hypereutectoid rail steels (HE1 for higher carbon content and HE2 for lower carbon content) with similar nominal hardness, were considered as an example of applying the developed approach for evaluating ratcheting performance of the rail steels. The influence of different cyclic rolling contact conditions, i.e. free rolling, full slip and partial slip, different friction coefficient and different axle load on the ratcheting performance of the three rail steels were investigated. The results can then provide useful information applicable to the selection of rail steels and the development of effective rail maintenance strategies for mitigating rail degradation.

The structure of this paper is as follows: the approach, which includes the significant findings of the experimental results, the developed ratcheting model for rail steels and the method of determining the crack initiation life, for evaluating the ratcheting performance of rail steels is given in Section 2. The finite element model and the methodology to determine the non-Hertzian normal pressure and the longitudinal tangential traction distributions are presented in Section 3. The numerical results of the ratcheting performance of the three rail steels under different service loading conditions are presented and discussed in Section 4. Conclusions are given in Section 5.

2. The comprehensive approach to evaluate ratcheting performance of rail steels

For the purpose of evaluating the ratcheting performance of rail steels under different loading conditions in service, a comprehensive

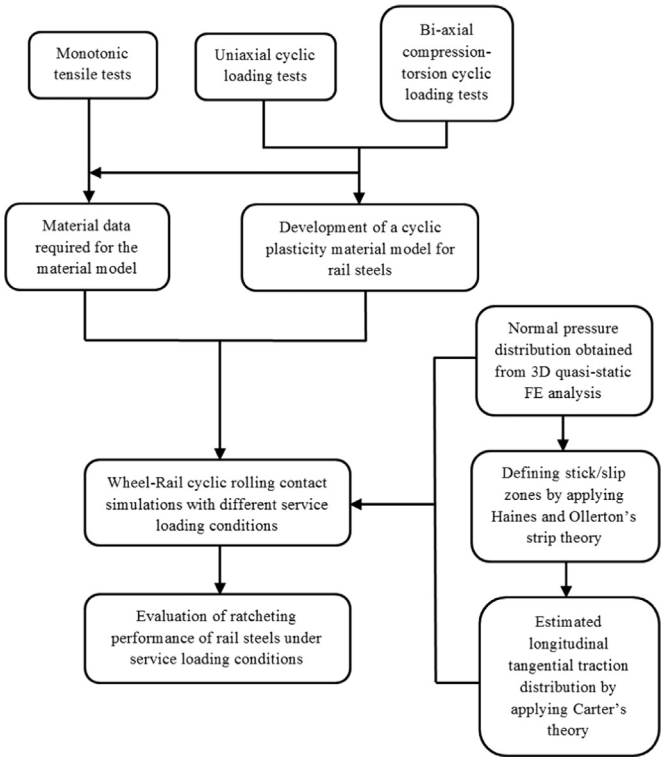

Fig. 1. Flowchart of the comprehesive approach to evaluate ratcheting performance of rail steels under service loading conditions.

approach has been developed and is illustrated in Fig. 1. This developed approach consists of a systematic experimental program; a developed cyclic plasticity material model for rail steels; the methodology of calibrating material parameters from the experimental results; and the methodology to numerically evaluate the ratcheting performance of rail steels under different loading conditions.

2.1. Experimental program

This developed approach starts with the experimental study on the ratcheting behaviour of rail steel materials. The major objective of conducting the experimental study was to investigate the uniaxial and bi-axial ratcheting behaviour of the rail steels subjected to cyclic loading. The systematic experimental programs, which included monotonic tensile tests, uniaxial strain and stress cycling tests, and non-proportional bi-axial stress cycling tests, was carried out recently by the authors to investigate the ratcheting behaviour of the three high strength rail steels considered herein [25]. Some significant findings from the experiments are briefly presented here. The details of the experimental program and results can be found in [25].

The experimental results showed that all the three studied rail steels have similar ratcheting behaviour. Under uniaxial symmetrical strain cycling, all the three rail steels exhibited cyclic softening, i.e. stress amplitude decreases with the increasing cyclic number, at the start and then stabilized quickly. Under uniaxial stress cycling, the ratcheting of all the three rail steels behaved slightly different under tension and compression. Under bi-axial compression-torsion stress cycling, the ratcheting behaviour of the three rail steels was significantly influenced by the axial stress and the equivalent shear stress amplitudes and the non-proportional loading path. For all the three rail steels, the ratcheting strain increases but the ratcheting strain rate decreased with the increasing cyclic number. After a certain number of loading cycles, a quasi-steady ratcheting strain rate was reached, i.e. cyclic stabilization was reached. All these features and their effect on ratcheting of the rail steels were then taken into account in the development of cyclic plasticity material model.

2.2. Ratcheting model for rail steels

Based on the experimental results, a ratcheting model, which can satisfactorily describe both uniaxial and non-proportional bi-axial ratcheting behaviour of the rail steels, was developed by the authors recently by coupling a non-proportional multi-axial parameter into isotropic softening and kinematic hardening rules [25]. Some major equations, i.e. the isotropic and kinematic hardening rules, adopted in the model are briefly presented here.

Based on the initial isotropic elasticity and associated plastic flow rules at small deformation, the plastic strain rate $\dot{\boldsymbol{\varepsilon}}^p$ and the von-Mises yield function F_y are described by,

$$\dot{\boldsymbol{\varepsilon}}^p = \sqrt{\frac{3}{2}}\dot{\lambda}\frac{\mathbf{s}-\boldsymbol{\alpha}}{\|\mathbf{s}-\boldsymbol{\alpha}\|} \tag{1}$$

$$F_y = \sqrt{1.5(\mathbf{s}-\boldsymbol{\alpha}):(\mathbf{s}-\boldsymbol{\alpha})} - Q \tag{2}$$

where $\mathbf{s}$ and $\boldsymbol{\alpha}$ are the deviatoric parts of stress and back stress. Q is the isotropic deformation resistance. $\dot{\lambda}$ is the rate of plastic multiplier. $\|\ \|$ denotes the norm.

Abdel-Karim and Ohno [32] proposed a kinematic hardening rule which combines the Armstrong and Frederick [33] and the Ohno and Wang [23] rules, and was adopted in the current study. The evolution equations of back stress for the kinematic hardening rule is shown as follows,

$$\boldsymbol{\alpha} = \sum_{i=1}^{M}\boldsymbol{\alpha}_i (i = 1, 2, \ldots, M) \tag{3}$$

$$\dot{\boldsymbol{\alpha}}_i = \zeta_i\left[\frac{2}{3}r_i\dot{\boldsymbol{\varepsilon}}^p - \mu_i\boldsymbol{\alpha}_i\dot{p} - H(f)_i\boldsymbol{\alpha}_i\left\langle\dot{\boldsymbol{\varepsilon}}^p : \frac{\boldsymbol{\alpha}_i}{\|\boldsymbol{\alpha}_i\|} - \mu_i\dot{p}\right\rangle\right] \tag{4}$$

where $\boldsymbol{\alpha}_i$ is components of back stress $\boldsymbol{\alpha}$, H is Heaviside function, $\langle\rangle$ is Macaulay's bracket and means that: as $x \le 0$, $\langle x\rangle = 0$; as $x > 0$, $\langle x\rangle = x.\dot{p}$ is the effective plastic strain rate. The critical state of dynamic recovery is described by the critical surfaces f_i:

$$f_i = \|\boldsymbol{\alpha}_i\|^2 - r_i^2 = 0 \tag{5}$$

The ratcheting parameter μ_i is assumed as a constant for different components of back stress.

$$\mu_i = \mu = \mu_0(1 - a\Phi) \tag{6}$$

where μ_0 is a ratcheting parameter in the uniaxial cases. a is a material parameter reflecting the influence of the non-proportional loading paths on ratcheting behaviour. Φ is the non-proportional parameter which associates with the non-proportionality of loading path [25].

Basically, the cyclic softening rule adopted in the cyclic plasticity model is used with the combined hardening model which considers both isotropic and kinematic hardening rules to capture the cyclic softening feature and the ratcheting behaviour. In order to consider the effects of loading history and non-proportional loading path, the following evolution equations for the isotropic deformation resistance Q are adopted in the constitutive model,

$$\dot{Q} = \gamma(Q_{sa} - Q)\dot{p} \tag{7a}$$

$$Q_{\mathrm{sa}}(\Phi) = \Phi[Q_{\mathrm{sa1}} - Q_{\mathrm{sa0}}] + Q_{\mathrm{sa0}} \tag{7b}$$

where $Q_{sa}(\Phi)$ is saturated isotropic deformation resistance relating to non-proportional factor Φ, and γ is a material parameter to control the evolution rate of Q_{sa}. Q_{sa0} and Q_{sa1} are the saturated isotropic deformation resistance under the cyclic loading paths for

$\Phi=0$ and $\Phi\approx 1$, respectively. The initial value of Q is denoted as Q_0.

To apply the ratcheting model to quantify plastic ratcheting of the rail steels, some of the material parameters required by the model were calibrated from the experimental data obtained from monotonic tensile tests and both uniaxial and biaxial cyclic loading tests. The details of how to calibrate those material parameters, i.e. the material constants ζ_i and r_i, can be found in [25]. The calibrated material data of the parameters used in the current study for the three rail steels with 8 back stresses are summarized in Table 2.

2.3. Evaluation of ratcheting performance

With the developed ratcheting model and the calibrated material parameters for the rail steels, the finite element method was then applied to simulate the wheel–rail cyclic rolling contact problems. Due to the multiaxial loading conditions in the rail head, the components of both normal and shear plastic strains accumulate during cyclic loading, i.e. ratcheting occurs. Therefore, the effective plastic strain $\varepsilon^p_{\text{eff}}$ in each loading cycle can be applied to investigate the ratcheting behaviour of the rail steel under cyclic rolling contact. It is defined in terms of the individual components of both normal and shear plastic strains by following the analogy with multiaxial fatigue analysis [34,35] as follows,

$$\varepsilon_r = \left(\varepsilon^p_{eff}\right)_{\max} = \left(\sqrt{\frac{2}{3}\boldsymbol{\varepsilon}^p : \boldsymbol{\varepsilon}^p}\right)_{\max} \tag{8}$$

where $\boldsymbol{\varepsilon}^p$ is the plastic strain tensor. Based on Eq. (8), the maximum effective plastic strain $(\varepsilon^p_{\text{eff}})_{\max}$ can be obtained in each loading cycle. As ratcheting is the accumulation of plastic deformation in each loading cycle, the maximum value of effective plastic strain $(\varepsilon^p_{\text{eff}})_{\max}$ obtained in each cycle can represent the ratcheting strain in multi-axial loading conditions in the rail head under wheel–rail cyclic rolling contact for investigating the ratcheting behaviour of the rail steel. In other words, the maximum effective plastic strain is the maximum ratcheting strain in each loading cycle as shown in Eq. (8). The ratcheting strain rate $d\varepsilon_r/dN$ is then represented by the rate of maximum effective plastic strain $d(\varepsilon^p_{\text{eff}})_{\max}/dN$, which is applied to estimate the crack initiation life of the rail steel in the rail head under different service loading conditions.

As discussed in the introduction, initiation of crack is primarily due to ratcheting. When the ratcheting strain reaches the ductility limit of the material, the material fails at its local material point which corresponds to initiation of rolling contact fatigue crack. According to this, the crack initiation life N_i of the rail steel can be applied to evaluate the ratcheting performance of the rail steels under different rolling contact conditions. The crack initiation life is estimated by the stabilized maximum ratcheting strain rate $(d\varepsilon_r/dN)_{\max,sta}$ and the ductility limit of the rail steel. The stabilized maximum ratcheting strain rate is the maximum ratcheting strain rate of the entire finite element rail model after the rail steel becomes cyclically stable, i.e. a constant rate of ratcheting strain is reached. In current study, a criterion, which is based on the rate of the maximum ratcheting strain rate, is applied to determine cyclically stable state,

$$\frac{(d\varepsilon_r/dN)_{\max,N}-(d\varepsilon_r/dN)_{\max,N-1}}{(d\varepsilon_r/dN)_{\max,N-1}} < 0.5\% \tag{9}$$

where $(d\varepsilon_r/dN)_{\max,N}$ is the maximum ratcheting strain rate in the current loading cycle and $(d\varepsilon_r/dN)_{\max,N-1}$ is the maximum ratcheting strain rate in the previous loading cycle. It is worth noting that the rail steel can only be determined as cyclically stable if the criterion, as shown in Eq. (9), is satisfied in 5 continuous cycles.

Under monotonic tensile test, the volume of the material within the gauge section is assumed to be constant. Therefore, the ductility limit D of the three rail steels can be determined by

$$D = \ln\left(\frac{L}{L_o}\right) = \ln\left(\frac{1}{1-R}\right) \tag{10}$$

where R is the reduction of area, which is the proportional reduction of the cross-sectional area of the specimen measured after fracture under the monotonic tensile test, of the three rail steels as shown in [25] and is also given in Table 1. Based on Eq. (10), the ductility limit of all three rail steels can be determined and are listed in Table 1. It is worth noting that the ductility of the rail steels can also be obtained from the twin-disc test [4,5] which is close to the actual wheel/rail rolling contact situation. However, due to the unavailability of the twin-disc test machine, the ductility limit was determined based on the reduction of area measured from the monotonic tensile tests in the current study; this approach was consistent with the work of Kapoor [5]. With the stabilized maximum ratcheting strain rate $(d\varepsilon_r/dN)_{\max,sta}$ and the ductility limit D, the crack initiation life N_i can then be estimated by,

$$N_i = \frac{D}{(d\varepsilon_r/dN)_{\max,sta}} \tag{11}$$

Table 1
Ductility limit of the three rail steels.

	LAHT	HE1	HE2
Reduction of area R (%)	35.87	14.71	39.5
Ductility limit D (%)	44.43	15.91	50.25

3. Finite element modelling

3.1. Contact pressure distribution

To simulate the wheel–rail cyclic rolling contact problems with different running modes, i.e. free rolling, partial slip and full slip conditions, different friction coefficients and different axle loads, both normal pressure distribution and tangential traction distribution were applied on the rail surface. Most of the existing literature applied the Hertzian contact pressure distribution to simulate the wheel–rail cyclic rolling contact problems. However, it has been found that the use of Hertzian normal pressure distribution can lead to discrepancies between the numerical results and reality due to the assumptions in Hertz contact theory, i.e. linear elastic material model and half-space assumption [2,14–18]. According to this, the non-Hertzian contact pressure was applied in this study. To determine the non-Hertzian contact pressure, the assumption of the distribution of contact pressure independent of the interfacial friction and shear forces was still employed. Johnson [36] stated that the interfacial friction plays a role in the normal contact only if two non-conformable bodies with dissimilar elastic properties are brought into contact. However, there is only a small loss of precision if the normal pressure is determined with the assumption of frictionless contact for two dissimilar deformable bodies [36]. Therefore, the non-Hertzian contact pressure distribution, which was obtained from a separate quasi-static finite element method with the assumption of normal pressure distribution independent of the friction coefficient, was applied in the current study. The numerical results of the non-Hertzian contact pressure were obtained at the nodes within the contact area of the numerical model. These values were then applied to determine the longitudinal

Table 2
Material data of the input parameters used in the ratcheting model for the three rail steels [25].

	HE1	HE2	LAHT
$\zeta_1, \zeta_2, \zeta_3, \zeta_4$	1820, 926, 498, 331	900, 389, 174, 90	1470, 3110, 1350, 556
$\zeta_5, \zeta_6, \zeta_7, \zeta_8$	188, 110, 77.5, 30.6	55.2, 41.3, 34.1, 24.4	286, 112, 80, 35.6
r_1, r_2, r_3, r_4 (MPa)	24.1, 83.6, 68.9, 62	109, 102, 62.4, 55.1	177, 23.1, 44.9, 53.3
r_5, r_6, r_7, r_8 (MPa)	66.9, 59.1, 31.2, 440	56.5, 69.1, 44.8, 194	56.2, 47.4, 35.3, 344
E (GPa), ν, μ_0	203, 0.33, 0.05	212, 0.33, 0.01	212, 0.33, 0.045
Q_0, Q_{sa0}, Q_{sa1} (MPa)	650, 400, 440	680, 550, 660	630, 460, 600
a, c, γ	0.7, 50, 2.0	0.7, 50, 1.0	0.7, 50, 2.0

tangential distribution. It is worth noting that the non-Hertzian contact pressure on the surface of each single element was then determined by averaging the corresponding nodal values of contact pressure as the size of the element is one cubic millimeter.

To consider the partial slip condition, the contact area was divided into slip and stick zones. In the slip zone, the tangential force is proportional to the normal pressure while both wheel and rail have identical micro-slip velocities in the stick zone. Therefore, it is required to identify the stick and slip zone for estimating the tangential traction. In current study, the Haines and Ollerton's strip theory [37] was applied to identify the stick and slip zone in the contact area. The philosophy of this theory is to divide the two-dimensional contact area into thin strips parallel to the rolling direction of the wheel by neglecting the interaction between adjacent strips. Therefore, the existing theories, i.e. Carter's theory [38], for determining the tangential traction for one-dimensional contact patch can be applied to every single strip. The capability of these theories has been verified by Johnson's study [36], which demonstrates that the estimated results satisfactory to the numerical results obtained from Kalker's theory [39]. In current study, the thin strips were defined based on the mesh width in the contact surface of the finite element rail model.

Fig. 2 shows an example of a strip, which is highlighted in red colour, defined in the contact area based on the finite element results. a_i is the semi-width of a strip along the x-axis. The strip, which has the longest semi-width, is then denoted by a_o. b_o is the longest semi-width of the contact area along the y-axis. Under steady-state rolling contact, the stick zone extends to the leading edge of the contact area where the material is approaching to be in contact [36,39,40]. The semi-width of the stick zone of each strip is then denoted as a_i', see Fig. 3. According to the contact theory [36], the size of the stick zone at the major width of the contact area a_o' is a function of the normalized tangential traction ξ, which is defined by,

$$\xi = \frac{|P_t|}{fL} \tag{12}$$

where P_t is the tangential force. f is the friction coefficient at the wheel–rail contact interface and L is the normal force which is the axle load in current study. Eq. (12) clearly demonstrates that the allowable tangential force P_t is limited by the product of the friction coefficient and the axle load. When $\xi=0$, it represents a free rolling case, i.e. the contact area consists of stick zone only. When $\xi=1$, the stick zone vanishes and it represents the full slip contact between the wheel and the rail. For a normal wheel–rail rolling contact operation, partial slip conditions, i.e. $0<\xi<1$, is commonly occurred. For instance, $\xi=0.5$ means that the traction transmitted takes half of the limiting capability for the driving elements.

Based on the strip theory, the relationship between the normalized tangential traction ξ and the size of stick zone at the major width of the contact area can be described by Eq. (13) and the numerical results are shown in Fig. 4 [37].

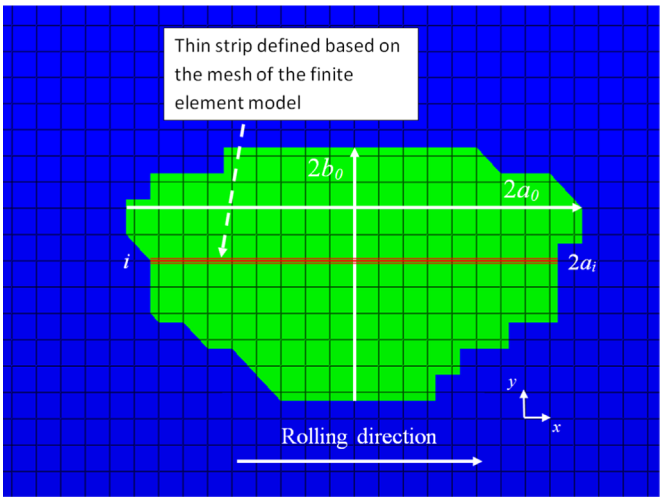

Fig. 2. Definition of strips within the contact area based on the structural mesh with identical element size of one cubic millimetre within the enlarged fine mesh region of the finite element model.

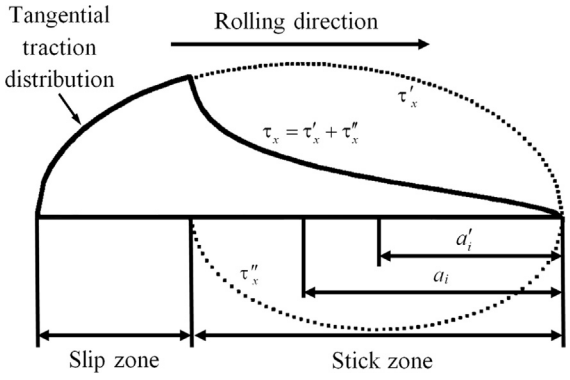

Fig. 3. Illustration of longitudinal tangential traction distribution in the stick and the slip zones of each strip.

$$\xi = 1 - \frac{3}{2} \times \left[\sqrt{2K-K^2}\left(1-\frac{2}{3}K+\frac{1}{3}K^2\right) - (1-K)\sin^{-1}\sqrt{2K-K^2}\right] \tag{13}$$

where $K = a_o'/a_o$ is the normalized size of stick zone at the major width of the contact area. If the normalized tangential traction ξ is known, the size of the stick zone at the major width of the contact area a_o' can be defined by either following Eq. (13) or using the numerical results in Fig. 4. After that, the size of the stick zone for each strip can be determined by following Eq. (14).

$$a_i - a_i' = a_o - a_o' \tag{14}$$

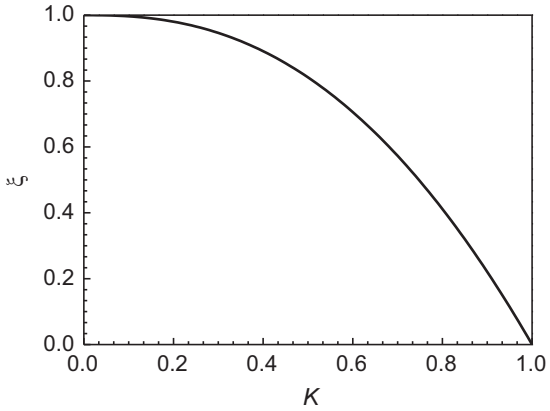

Fig. 4. Relationship between the normalized tangential traction ξ and the normalized size of stick zone K at the major width of the contact area [36].

For a two-dimensional contact patch, the semi-width of the stick zone along the y-axis b_o' is also required for accurate identification of the stick/slip zones and it is determined by,

$$b_o' = b_o\sqrt{\left[2\frac{a_o'}{a_o} - \left(\frac{a_o'}{a_o}\right)^2\right]} \tag{15}$$

Based on the coordinates of the nodes within the contact area of the finite element model, the nodes in the stick zone are identified when $a_i - 2a_i' \le x \le a_i$ and $y \le b_o'$ while those in the slip zone are identified when $-a_i \le x \le a_i - 2a_i'$ and $b_o' < y \le b_o$. With the defined stick/slip zones, the tangential traction distribution in the stick and slip zones of the contact area can then be estimated by following the Carter's theory [38].

$$\tau_x(x_i, y_i) = fp(x_i, y_i) - \frac{a_i'}{a_i} fp(x_i, y_i) \quad \text{for} \quad a_i - 2a_i' \le x \le a_i \quad \text{and} \quad y \le b_o' \tag{16}$$

$$\tau_x(x_i, y_i) = fp(x_i, y_i) \quad \text{for} \quad -a_i \le x \le a_i - 2a_i' \quad \text{and} \quad b_o' < y \le b_o \tag{17}$$

where $\tau_x(x_i, y_i)$ is the longitudinal tangential traction. It is worth noting that only the longitudinal tangential traction was considered as current study focus on investigating the ratcheting performance of the rail steel under different wheel–rail rolling conditions on a tangent track. Therefore, it is assumed that the lateral tangential traction is significantly small and can be neglected. $p(x_i, y_i)$ is the nodal values of non-Hertzian contact pressure obtained from the quasi-static frictionless finite element analysis as described earlier. f is the friction coefficient. Several values of friction coefficient, i.e. $0.2 \le f \le 0.6$, were considered in order to investigate the influence of different friction coefficients on the ratcheting performance of the three rail steels in this study.

The longitudinal tangential tractions determined in Eqs. (16) and (17) are the nodal values along the strips within the contact area. These nodal values were then converted to the longitudinal tangential traction on the surface of every single element within the contact area by averaging the corresponding nodal values as the size of the element is one cubic millimeter. As an example, the nodal values of contact pressure distribution obtained from the finite element analysis for the LAHT steel with axle load of 35 t is illustrated in Fig. 5a while the determined nodal values of longitudinal tangential traction with the normalized tangential traction of $\xi = 0.5$; $\xi = 0.75$; and $\xi = 1.0$ for the LAHT steel with axle load of 35 t and friction coefficient of 0.4 are shown in Fig. 5b–d.

Ideally, the normal pressure and tangential traction distributions should be directly obtained from a dynamic finite element simulation. However, a very long segment of rail with a fine mesh, a full wheel with a fine mesh and an extremely small time increment are required to simulate the dynamic wheel/rail rolling process starting from a transient stage to a steady stage, which will require not only significant computation costs but also elegant considerations in order to obtain satisfactory results. The current approach used the numerical results from a computationally inexpensive quasi-static finite element simulation and combined

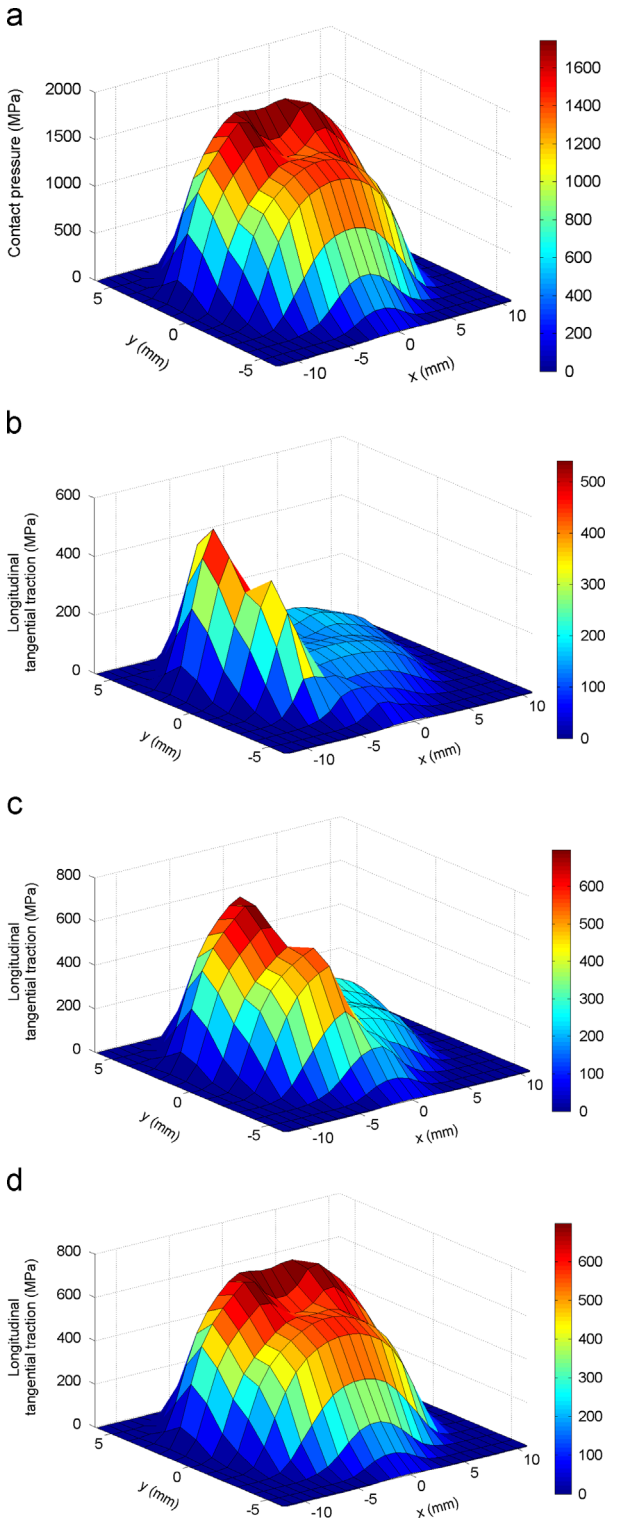

Fig. 5. (a) Contact pressure distribution; and longitudinal tangential traction distribution with different normalized tangential traction, (b) $\xi = 0.5$; (c) $\xi = 0.75$; (d) $\xi = 1.0$, for the LAHT steel with axle load of 35 t and friction coefficient of 0.4.

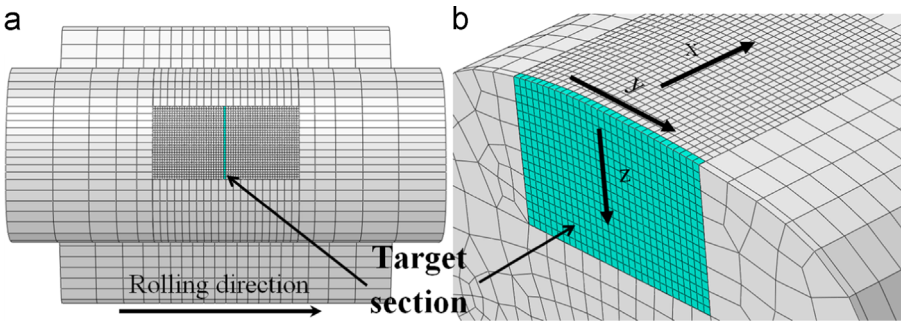

Fig. 6. (a) Finite element model; and (b) Finite element mesh in the contact region for simulating wheel–rail cyclic rolling contact.

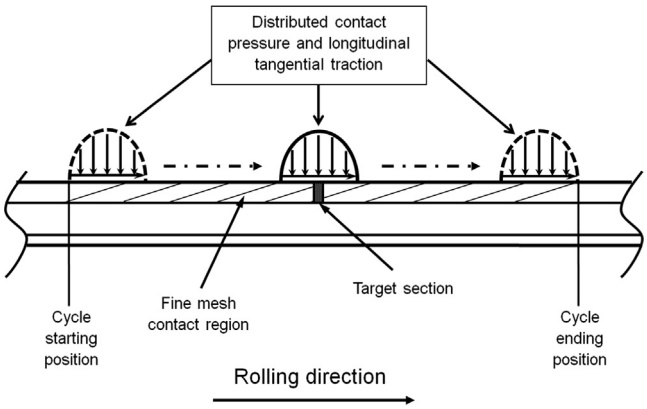

Fig. 7. Schematic illustration of the moving contact load distributions on the rail surface in a loading cycle.

with the Haines and Ollerton's strip [37] and Carter [38] theories to determine the contact pressure and the tangential traction distributions, which is a cost effective and practical feasible approach.

3.2. Numerical model for wheel–rail cyclic rolling contact

The commercial finite element software package, Abaqus, was applied to simulate the wheel–rail cyclic rolling contact problems. Due to the nature of three-dimensional rolling contact between the wheel and the rail, no symmetry can be found. Therefore, a full three-dimensional finite element model was developed as shown in Fig. 6. The three-dimensional rail model was generated by extruding the two-dimensional rail profile of a flat bottom rail, which has the crown radius of 254 mm and gauge radius of 31.75 mm. This rail model represents 180 mm of a track and is divided into two parts, the fine mesh contact zone and the coarse mesh zone. The fine mesh contact zone is generated for capturing the high stress and strain gradients near the rolling contact surface. It incorporates 60 mm long and 30 mm width of the top of the railhead, and it is defined to a depth of 18 mm which is three times larger than the contact area in all three directions. Structural mesh with element size of one cubic millimetre was applied and there are 32,400 elements and 35,929 nodes within the fine mesh contact zone. The surface-based mesh tie constraint is applied to connect the fine mesh contact zone and the coarse mesh zone. The entire finite element model consists of 41450C3D8 elements and it has 142,581 degrees of freedom in total. The cyclic plasticity material model for ratcheting developed recently by the authors with the calibrated material parameters [25] was applied to define the material properties of the entire finite element rail model.

Fig. 7 demonstrates the schematic illustration of the moving load distributions on the rail surface in a loading cycle. The wheel–rail cyclic rolling contact was simulated by repeatedly translating the distributed normal pressure and the distributed tangential traction on the rail surface from left to right of the fine mesh contact zone. The translation of both normal pressure distribution and longitudinal tangential traction distribution was modelled by the time-dependent amplitude function with fixed time interval [41] of every contact element within the fine mesh contact zone. Throughout the simulation, all the nodes at the bottom of the rail are pinned, i.e. movement in all three directions were constrained. For an idealized wheel–rail rolling contact on a straight track, any material points with identical coordinates in the y and z direction have the identical stress and strain responses. This implies that both stresses and strains are independent of the coordinates in the x direction. Therefore, all the results presented below were obtained from a target section, which is located at the centre of the fine mesh contact zone as shown in Fig. 6.

4. Numerical results and discussion

With the developed ratcheting model for rail steels and the numerical rail model for cyclic rolling contact simulations, several case studies on the ratcheting performance of the three rail steels under different wheel–rail cyclic rolling contact conditions, i.e. free rolling, partial slip, and full slip conditions, different friction coefficients and different axle loads were conducted. The number of cycles performed in each case depends on the number of loading cycles required for the rail to reach cyclically stable state.

Fig. 8 shows the maximum ratcheting strain rate $(d\varepsilon_r/dN)_{\max}$ versus number of loading cycle N with different values of normalized tangential traction ξ for all the three rail steels. The results clearly illustrate that the maximum ratcheting strain rate increases with the normalized tangential traction for all the three rail steels but decreases with the increasing cyclic number N. Additionally, it is found that the number of loading cycles required to become cyclically stable, i.e. the criterion as demonstrated in Eq. (9) is satisfied, is significantly influenced by the normalized tangential traction ξ. Although the materials become cyclically stable, non-zero stabilized maximum ratcheting strain rate is still obtained in all the considered cases for all three rail steels. This indicates that non-zero net plastic deformation is still accumulating in every cycle, i.e. ratcheting. For all three rail steels, the stabilized maximum ratcheting strain rate is in the range of 10^{-7} when the normalized tangential traction is less than or equal to 0.5. When the normalized tangential traction increases to 0.75, the LAHT steel has the highest stabilized maximum ratcheting strain rate of 9.9×10^{-6} while it is 2.5×10^{-6} and 5×10^{-7} for the LAHT and the HE2 steels, respectively. Under the full slip condition, i.e. $\xi=1$, the stabilized maximum ratcheting strain rate for the HE1 steel

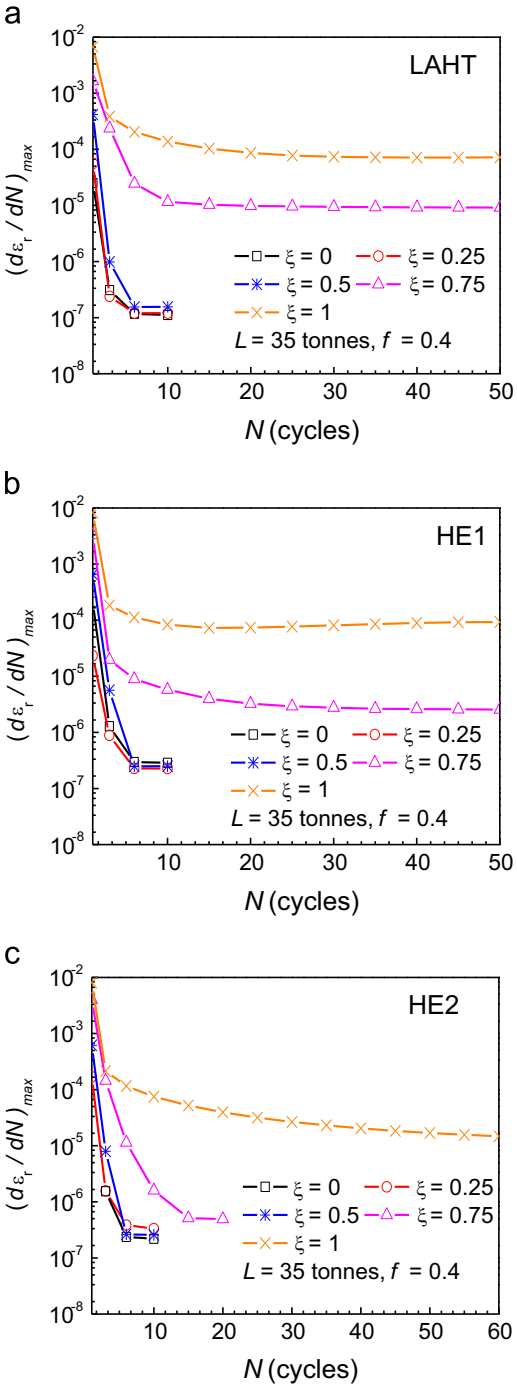

Fig. 8. Maximum ratcheting strain rate $(d\varepsilon_r/dN)_{\max}$ versus number of loading cycle N under different values of normalized tangential traction ξ for (a) LAHT steel; (b) HE1 steel; and (c) HE2 steel, with axle load L of 35 t and friction coefficient f of 0.4.

increases to 7.4×10^{-5} while it is 7.2×10^{-5} and 1.5×10^{-5} for the LAHT and the HE2 steels, respectively. This show that the HE2 steel always has the lowest stabilized maximum ratcheting strain rate among all the three rail steels in all these considered cases. Although the stabilized maximum ratcheting strain rate is very small, the non-zero net plastic deformation can accumulate to a very large value over millions of loading cycle and lead to initiation of fatigue crack, i.e. ratcheting damage [4]. Therefore, the stabilized maximum ratcheting strain rate can be applied to estimate the crack initiation life of the rail steels by Eq. (12).

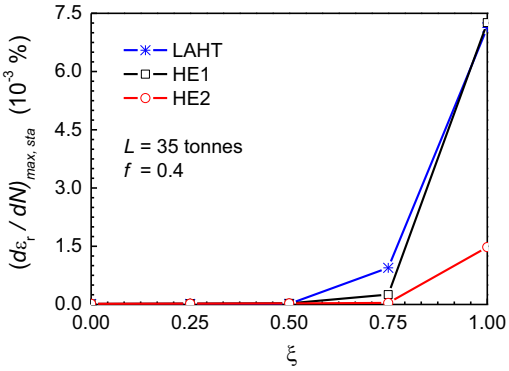

Fig. 9. Stabilized maximum ratcheting strain rate $(d\varepsilon_r/dN)_{\max,sta}$ versus the normalized tangential traction ξ for all the three rail steels with axle load L of 35 t and friction coefficient f of 0.4.

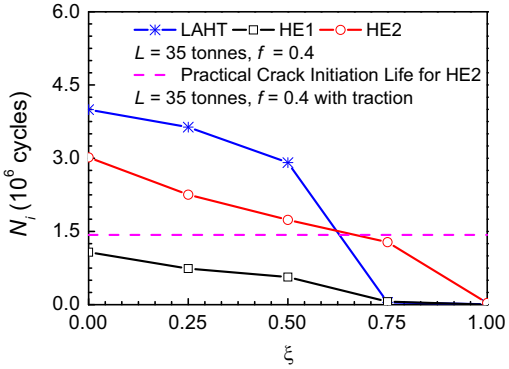

Fig. 10. Estimated crack initiation life N_i versus normalized tangential traction ξ for all the three rail steels with axle load L of 35 t and friction coefficient f of 0.4.

Fig. 9 shows the stabilized maximum ratcheting strain rate $(d\varepsilon_r/dN)_{\max,sta}$ obtained for different values of the normalized tangential traction for all the three rail steels. The results illustrate that the stabilized maximum ratcheting strain rate for all three rail steels is almost constant when the normalized tangential traction is less than or equal to 0.5. When the normalized tangential traction further increases, a rapid increase on the stabilized maximum ratcheting strain rate is observed for both LAHT and HE1 steels. In comparison, the influence of the normalized tangential traction on the stabilized maximum ratcheting strain rate for HE2 steel is minor although the normalized tangential traction is larger than 0.5. Among all the three rail steels, the magnitude of the stabilized maximum ratcheting strain rate for all three rail steel is almost identical when the normalized tangential traction is less than or equal to 0.5. When the normalized tangential traction is larger than 0.5, the HE2 steel gives the lowest stabilized maximum ratcheting strain rate.

With the stabilized maximum ratcheting strain rate as shown in Fig. 9 and the ductility limit as listed in Table 1, the crack initiation life N_i of the three rail steels under different normalized tangential traction ξ can be estimated by following Eq. (12). Fig. 10 illustrates the influence of the normalized tangential traction ξ on the crack initiation life N_i for all the three rail steels. The results clearly demonstrate that the crack initiation life decreases with the increase of the normalized tangential traction. Under the free rolling conditions, i.e. $\xi=0$, the crack initiation life of LAHT steel is up to 4 million cycles, while it is 1.1 million cycles and 3 million cycles for the HE1 and the HE2 steels, respectively. When partial slip conditions occur, i.e. $0<\xi<1$, the crack initiation life is significantly reduced. For the LAHT steel, a rapid reduction of crack initiation life is found when the normalized tangential

traction is larger than 0.5. For both HE1 and HE2 steels, a more constant decreasing rate of the crack initiation life is observed under the partial slip conditions. When the normalized tangential traction equals to 1, i.e. full slip condition, the crack initiation life for both LAHT and HE1 steels is less than 10^4 cycles while the crack initiation life for HE2 steel is just reduced to 10^5 cycles. Among all the three rail steels, the HE1 steel has the shortest crack initiation life among all the three rail steels. The LAHT steel has the longest crack initiation life under low traction conditions, i.e. $\xi \leq 0.5$, while the HE2 steel has the longest crack initiation life under high traction conditions.

In practice, minor surface cracks can be found in the rail head after the traffic of 50 million gross tonnes on average in a straight track, where the HE2 steel is installed, subjected to an average axle load of 35 t with an average friction coefficient of 0.4 and tractive force. It is worth noting that this average traffic tonnage for HE2 steel was obtained from the field investigation in Pilbara, West Australia. The practical results of the crack initiation life of the HE2 steel can then be estimated by dividing the average traffic by the average axle load. It is about 1.4 million cycles and is illustrated by the pink dash line in Fig. 10. The results demonstrate that the numerical results of the HE2 steel are in line with the practical results especially when the normalized tangential traction lies between 0.5 and 0.75, where the difference is less than 5%. It is worth noting that the normalized tangential traction is normally lies between 0 and 1 in actual wheel–rail rolling contact situations. According to this, the normalized tangential traction of 0.5 is chosen for the investigation of the influence of friction coefficient and axle load on the crack initiation life of the three rail steels.

The influence of different friction coefficient f on the ratcheting performance of the three rail steels was also investigated in current study. Fig. 11 demonstrates the maximum ratcheting strain rate $(d\varepsilon_r/dN)_{\max}$ versus number of loading cycle N with different values of friction coefficient f for all the three rail steels. The results show that the maximum ratcheting strain rate increases with the friction coefficient but decreases with the increasing cyclic number for all the three rail steels. It is also found that the number of loading cycles required to become cyclically stable is significantly influenced by the friction coefficient. It is worth noting that non-zero stabilized maximum ratcheting strain rate is also obtained in all the cases for all three rail steels. When the friction coefficient is less than or equal to 0.5, all three rail steels have the stabilized maximum ratcheting strain rate in the range of 10^{-7}. When the friction coefficient increases to 0.6, the stabilized maximum ratcheting strain rate for both LAHT and HE1 steels dramatically increase to 10^{-5} while it is just increase to 10^{-6} for the HE2 steel.

Fig. 12 shows the stabilized maximum ratcheting strain rate $(d\varepsilon_r/dN)_{\max\_sta}$ for different friction coefficient f for all the three rail steels. The results demonstrate that the stabilized maximum ratcheting strain rate for all three rail steels is almost constant when the friction coefficient is less than or equal to 0.4. When the friction coefficient increases to 0.5, slight increase on the stabilized maximum ratcheting strain rate is found for the LAHT steel while there is no significant influence on the stabilized maximum ratcheting strain for both HE1 and HE2 steels. Further increase of the friction coefficient causes a rapid increase on the stabilized maximum ratcheting strain rate for both LAHT and HE1 steels. In comparison, the influence of the friction coefficient on the stabilized maximum ratcheting strain rate for the HE2 steel is minor. The stabilized maximum ratcheting strain rate for all three rail steels is almost identical when the friction coefficient is less than or equal to 0.4. When the friction coefficient is larger than 0.5, the HE2 steel gives the lowest stabilized maximum ratcheting strain rate while both LAHT and HE1 steels have identical stabilized maximum ratcheting strain rate.

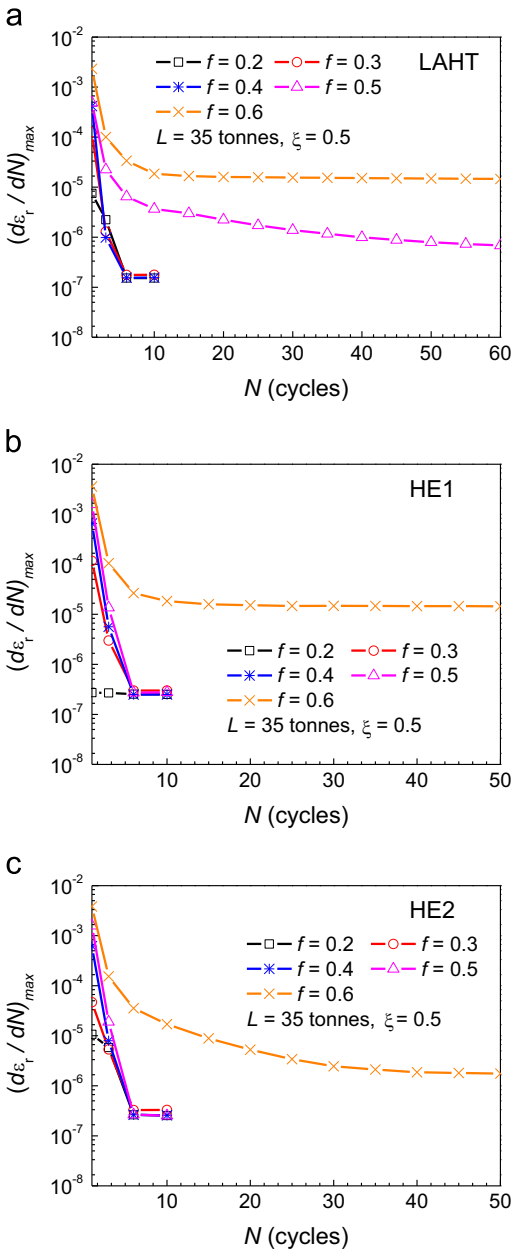

Fig. 11. Maximum ratcheting strain rate $(d\varepsilon_r/dN)_{\max}$ versus number of loading cycle N with different values of friction coefficient f for (a) LAHT steel; (b) HE1 steel; and (c) HE2 steel, with axle load L of 35 t and normalized tangential traction ξ of 0.5.

The influence of friction coefficient f on crack initiation life N_i for all the three rail steels is demonstrated in Fig. 13. The results clearly show that the crack initiation life decreases with the increase of the friction coefficient. When friction coefficient equals to 0.2, the LAHT steel has the longest crack initiation life of 3.5 million cycles, while it is 0.8 million cycles and 2.2 million cycles for the HE1 and the HE2 steels, respectively. When the friction coefficient is less than or equal to 0.4, the LAHT steel has the longest crack initiation life while the HE1 steel has the shortest one among all the three rail steels. However, the crack initiation life for the LAHT steel is reduced by 78% when the friction coefficient increases from 0.4 to 0.5. Under these conditions, the HE2 steel has the longest crack initiation life among all the three rail steels. When the friction coefficient further increases to 0.6, the crack initiation life for the LAHT steel is reduced to 10^4 cycles which is almost identical to that for the HE1 steel. Among all three

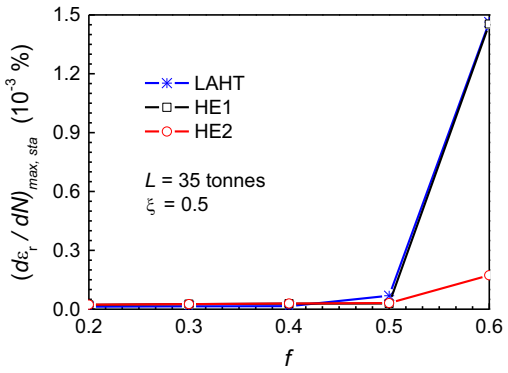

Fig. 12. Stabilized maximum ratcheting strain rate $(d\varepsilon_r/dN)_{max,sta}$ versus friction coefficient f for all the three rail steels with axle load L of 35 t and normalized tangential traction ξ of 0.5.

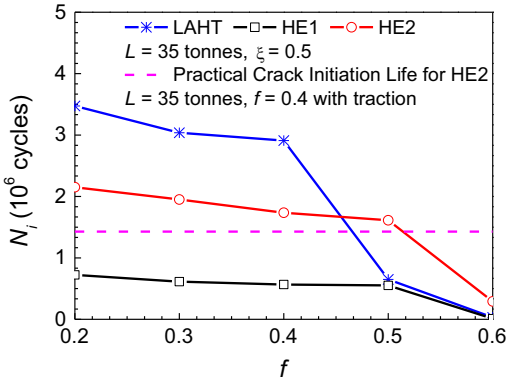

Fig. 13. Estimated crack initiation life N_i versus friction coefficient for all the three rail steels with axle load L of 35 t and normalized tangential traction ξ of 0.5.

rail steels, both HE1 and HE2 steels have a relatively consistent decreasing rate of crack initiation life when friction coefficient is less than or equal to 0.5. These results reveal that the use of LAHT steel requires a more appropriate control of friction between the wheel and the rail in order to mitigate the development of fatigue damage.

In Australia, the axle load for coal haulage vehicles is normally 30 t while those for iron ore haulage are typically in the range of 35–40 t. To fulfil the demanding conditions in heavy haul railway, increasing the axle load of the haulage vehicles may be required, i.e. an increase from 40 to 45 t. Therefore, it is also essential to understand the ratcheting performance of the rail steels under different service loading conditions. The results of the maximum ratcheting strain rate $(d\varepsilon_r/dN)_{max}$ versus number of loading cycle N under different axle load L for the three rail steels are demonstrated in Fig. 14. The results show that the maximum ratcheting strain rate increases with the axle load for all three rail steels. All the three rail steels give a non-zero stabilized maximum ratcheting strain rate although cyclically stable is reached. For the LAHT steel, the stabilized maximum ratcheting strain rate is in the range of 10^{-7} when the axle load is less than or equal to 35 t. When the axle load increases to 40 and 45 t, the stabilized maximum ratcheting strain rate rapidly increases to almost 10^{-5}. In comparison, the influence of axle load on the stabilized maximum ratcheting strain rate for both HE1 and HE2 steels is insignificant. In all the considered cases, the stabilized maximum ratcheting strain rate for both HE1 and HE2 steels lies between 2.5×10^{-7} and 3×10^{-7}.

Fig. 15 summarizes the stabilized maximum ratcheting strain rate $(d\varepsilon_r/dN)_{max,sta}$ obtained under different axle load L for all the three rail steels. The results demonstrate that the stabilized

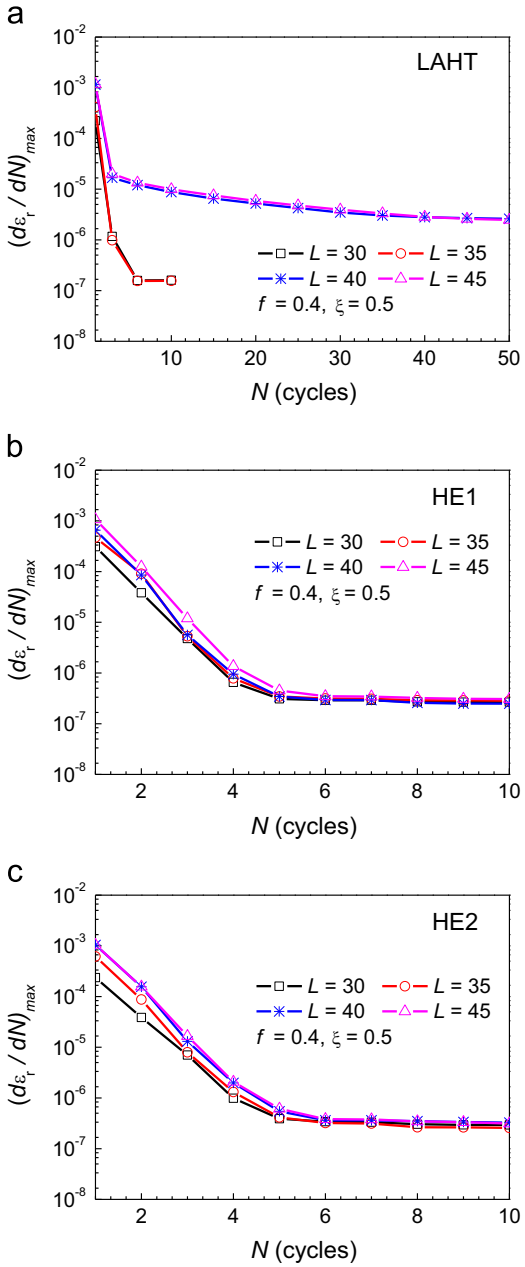

Fig. 14. Maximum ratcheting strain rate $(d\varepsilon_r/dN)_{max}$ versus number of loading cycle N under different axle load L for (a) LAHT steel; (b) HE1 steel; and (c) HE2 steel, with friction coefficient f of 0.4 and normalized tangential traction ξ of 0.5.

maximum ratcheting strain rate for both HE1 and HE2 steels is almost constant. When the axle load is less than 40 t, the stabilized maximum ratcheting strain rate for both HE1 and HE2 steels is almost identical and the LAHT steel gives the lowest stabilized maximum ratcheting strain rate. When the axle load increases to 40 t, the stabilized maximum ratcheting strain rate for LAHT steel increases rapidly and it gives the highest stabilized maximum ratcheting strain rate while the HE1 steel gives the lowest stabilized maximum ratcheting strain rate.

The estimated crack initiation life N_i under different axle load L for all the three rail steels is shown in Fig. 16. The results demonstrate that the crack initiation life decreases with the increase of axle load although the influence on the crack initiation life for the HE1 steel is not significant. When axle load is less than or equal to 35 t, the LAHT steel has the longest crack initiation life while the HE1 steel has the shortest one among all the three rail

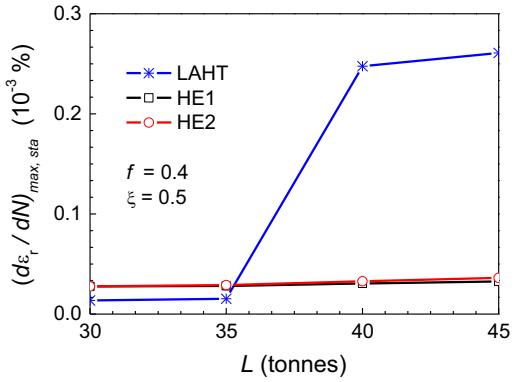

Fig. 15. Stabilized maximum ratcheting strain rate $(d\varepsilon_r/dN)_{\max,sta}$ versus axle load L for all the three rail steels with friction coefficient f of 0.4 and normalized tangential traction ξ of 0.5.

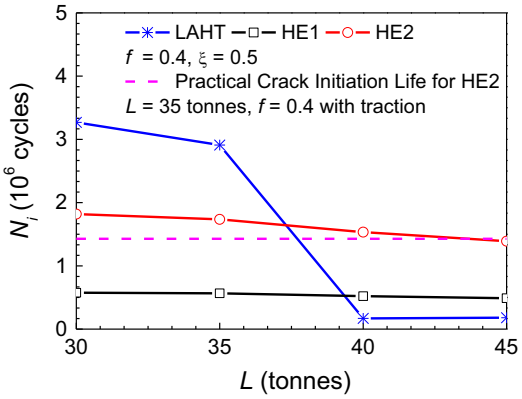

Fig. 16. Estimated crack initiation life N_i versus axle load L for all the three rail steels with friction coefficient f of 0.4 and normalized tangential traction ξ of 0.5.

steels. When the axle load increases from 35 to 40 t, the crack initiation life for the LAHT steel is reduced by 90%. Since then, the HE2 steel has the longest crack initiation life and the LAHT steel has the shortest crack initiation life among all the three rail steels. In comparison, both HE1 and HE2 steels have a relatively constant decreasing rate of crack initiation life. These reveal that the LAHT steel has the best performance than the two hypereutectoid rail steels under lower loading conditions and vice versa.

Figs. 8, 11, and 14 demonstrate that the decreasing ratcheting strain rate leads to plastic shakedown under wheel–rail cyclic rolling contact for all the three rail steels when the normalized tangential traction ξ; friction coefficient f; and axle load L is relatively low, i.e. $\xi \leq 0.5$; $f \leq 0.4$; and $L \leq 35$ t. If the normalized tangential traction, friction coefficient and axle load is relatively high, the ratcheting strain increases but its rate decreases continuously with increasing number of loading cycles. After a certain number of loading cycles, a stabilized maximum ratcheting strain rate is obtained, i.e. criterion as shown in Eq. (9) is satisfied. It is also found that the increase of normalized tangential traction, friction coefficient and axle load leads to an increase in the required cyclic number to become cyclically stable. Besides, the required cyclic number to become cyclically stable in different material is found to be different. This indicates that the required number of loading cycle for becoming cyclically stable also depends on the material properties. Referring to the calibrated material parameters of the three rail steels presented in [25], it is found that the material, which gives a lower cyclic yield strength, i.e. the initial isotropic deformation resistance Q_0, requires a larger cyclic number to become cyclically stable.

Figs. 9, 12, and 15 illustrate that the increase of normalized tangential traction, friction coefficient and axle load leads to an increase in the stabilized maximum ratcheting strain rate. It is also found that the increasing rate of the stabilized maximum ratcheting strain rate depends on not only the rolling contact conditions but also the material properties. For instance, a rapid increase on the stabilized maximum ratcheting strain rate for the LAHT steel is observed when axle load is larger than 35 t, while both HE1 and HE2 steels have a relatively constant increasing rate of the stabilized maximum ratcheting strain rate with the axle load. Similar phenomenon for the LAHT steel is also found when the friction coefficient is larger than 0.4 or the normalized tangential traction is larger than 0.5. This can be explained as the ratcheting behaviour of a material strongly depends on its cyclic hardening/softening features [42,43]. According to the study by Stephens et al. [44], the tendency for cyclic softening/hardening of a material is influenced by its microstructure. For hardened or initially hard material, the existing dislocation structure rearranges into a configuration with less resistance to deformation under cyclic loading and leads to promote greater dislocation mobility. In this case, dislocations are able to circumnavigate around microstructural barriers, i.e. precipitates and grain boundaries, which generally restrict deformation [44]. Therefore, the hardened or initially hard materials exhibit cyclic softening and the cyclic yield strength is smaller than the monotonic yield strength, i.e. $\sigma_{ys}/\sigma_y < 1$. All three high strength rail steels studied herein are pearlitic head-hardened rail steels, and have the cyclic yield strength lower than their monotonic yield strength, see [25]. Among all the three rail steels, the LAHT steel has the lowest ratio of σ_{ys}/σ_y of 0.63 while it is 0.76 and 0.75 for the HE1 and the HE2 steels, respectively. This indicates that the LAHT steel is more sensitive to cyclic softening than the two hypereutectoid rail steels. Therefore, the LAHT steel may suffer higher degrees of plastic deformation and require more cyclic number to become cyclically stable than the HE1 and the HE2 steels when the wheel–rail rolling contact conditions is more severe, i.e. high traction and high axle load conditions. It is worth noting that both the wheel and the rail are profiled to ensure conformal contact in accordance to the loading conditions, the material behaviour and the railway operator's requirements after installation in practice. However, the profiles of both wheel and rail were not changed with the loading conditions in the current study. This limitation can also lead to the sudden reduction of the crack initiation life of the LAHT steel under high axle load conditions.

As the crack initiation life is estimated based on the stabilized maximum ratcheting strain rate, this reveals that the possible location of crack initiation should be the same as the location of the stabilized maximum ratcheting strain rate. According to the numerical results, the stabilized maximum ratcheting strain rate is always located within a radius of 3 mm from the initial contact point. This indicates that the possible location of crack initiation should be within a depth of 3 mm from the running surface of the rail head. Typically, a rolling contact fatigue crack is originated from either a small surface crack or a sub-surface crack which is within 5 mm depth from the running surface of the rail head [45]. This implies that the current results agree with the practical investigation. Therefore, the information provided herein will be useful for the development of rail grinding technique, i.e. proportions of rail head to be removed in grinding process, in order to maintain the performance of the rail track.

Based on the numerical results of the stabilized maximum ratcheting strain rate and the ductility limit of the three rail steels, which was determined from the reduction of area, the crack initiation life of the three rail steels under different wheel–rail rolling contact conditions have been demonstrated in Figs. 10, 13, and 16. Among all the three rail steels, the LAHT steel has best resistance to ratcheting

and the longest crack initiation life when the rolling contact condition is mild, i.e. $\xi \leq 0.5$; $f \leq 0.4$; and $L \leq 35$ t. When the rolling contact condition becomes more severe, the LAHT steel has the shortest crack initiation life than the two hypereutectoid rail steels. This indicates that the LAHT steel may not be able to be applied in high traction area of the rail track in practice. Additionally, the LAHT steel may not be a good choice when comparing to the two hypereutectoid rail steels if the axle load is intended to increase to 40 or even 45 t to fulfil the demanding conditions imposed by heavy haul rail transport with higher axle loads in Australia. Besides, more effort must be made to control the friction at the interface between the wheel and the rail in order to maintain the performance of rail track although the LAHT steel may still be able to apply in the area with lower axle load and lower traction.

The HE1 steel, which has the carbon content of 1%, shows a relatively worse resistance to ratcheting and relatively shorter crack initiation life when comparing to the HE2 steel, which has the carbon content of 0.85%. Although the HE1 steel gives the lowest stabilized maximum ratcheting strain rate under high axle load, i.e. $L \geq 40$ t, the crack initiation life of the HE1 steel is still much shorter than that of the HE2 steel due to its lower ductility limit. As shown in Table 1, the ductility limit of the HE1 steel is 68% less than that of the HE2 steel. This indicates that the increase of carbon content of a hypereutectoid rail steel significantly reduces its ductility limit and its crack initiation life although its resistance to ratcheting under higher loading conditions can be slightly improved. It is worth noting that a more frequent maintenance may be required if the HE1 steels is installed in the heavy haul railway track. This can increase the maintenance cost of the railway. Therefore, it is necessary to strike a balance between the carbon content and the crack initiation life of the material when developing new high strength rail steels in the future.

Practically, a rail suffers variation of cyclic rolling contact conditions throughout its service life. Therefore, a consistent resistance to ratcheting and crack initiation life of the rail under different wheel–rail rolling contact conditions plays an important role on extending the service life of a rail. Among all the three rail steels, the HE2 steel has the lowest stabilized ratcheting strain rate and the longest crack initiation life in most of the cases, especially under high traction and high axle load conditions. Additionally, the HE2 steel has the most consistent resistance to ratcheting and the most consistent crack initiation life under all considered loading conditions. Therefore, the HE2 steel should be the best one to apply in heavy haul railway among all the three rail steels. Also, it is the most potential one to be applied in track for increasing axle load.

The crack initiation life for the HE2 rail steel estimated from the field investigation in Pilbara, West Australia under an averaged axle load of 35 t and friction coefficient of 0.4 with tractive force on a straight track is illustrated by the pink dashed line in Figs. 10, 13 and 16. It shows that the numerical results give a reasonable prediction on the crack initiation life of the rail steel although some discrepancies are still found between the numerical estimation and the practical estimation. Practically, the transverse location of the initial contact point varies during the wheel–rail rolling contact due to the presence of transverse shear force. However, the transverse shear force is still much lower than the longitudinal shear force on a straight track. Additionally, the rail suffers varying friction coefficient and loads throughout its service life while constant axle load and constant friction coefficient are considered in current study. Despite these, the differences between the numerical results and the practical results of crack initiation life is less than 15% in most of the cases while some of them is as low as 3% only. All the three rail steels studied herein were also included in a larger range of rail steels subjected to an in-service testing by Szablewski et al. [46,47]. The rails were tested with axle load of 35 t and tractive force under dry friction conditions. Their results indicate that the LAHT steel has the largest wear area and more severe rolling contact fatigue damage, i.e. in the form of head check, when comparing to the two hypereutectoid rail steels after the traffic of 348 million gross tonnes. This indicates that the numerical results obtained from the proposed approach give a reasonable agreement with the in-service performance of the three rail steels.

According to this, the approach developed for evaluating the ratcheting performance of the rail steels in current study with the developed cyclic plasticity material model and the calibrated material parameters can also be applied to estimate the crack initiation life of the three rail steels in other section of the rail track, i.e. the curved track. Additionally, this approach, which includes the systematic experimental program, the developed ratcheting model for rail steels and the methodology of evaluating ratcheting performance, can also be applied to evaluate the ratcheting performance of other pearlitic rail steels under actual wheel–rail cyclic rolling contact conditions. The results can then provide useful information to railway operators for the development of a reliable and cost-effective rail maintenance strategy for a specific rail track and for rail steel producers to develop high performance rail steels.

5. Conclusions

A comprehensive approach to numerically evaluate ratcheting performance of rail steels has been developed in this study. Three high strength pearlitic rail steels, which have been examined by the authors recently, were considered in a comprehensive study to evaluate their ratcheting performance under different wheel–rail cyclic rolling contact conditions. This study combined the non-Hertzian contact pressure from the finite element analysis with the longitudinal tangential traction from Carter's theory to simulate the wheel–rail cyclic rolling contact problems. The influence of different normalized tangential traction, friction coefficients and axle loads on the ratcheting behaviour and the crack initiation life of the three rail steels have been investigated. The numerical results demonstrate that the maximum ratcheting strain increased but its rate decreased continuously with increasing number of loading cycles. After a certain number of loading cycles, the materials reached cyclically stable and a non-zero stabilized maximum ratcheting strain rate was obtained in all the considered cases. This indicates that non-zero net plastic deformation is still accumulating in every loading cycle and lead to crack initiation once the ratcheting strain reaches the ductility limit of the rail steels, i.e. ratcheting damage, although the materials have become cyclically stable. Therefore, the stabilized maximum ratcheting strain rate and the ductility limit of the rail steels were then applied to estimate the crack initiation life of the three rail steels for the corresponding rolling contact condition.

The numerical results show that the crack initiation life of all three rail steels decreases with the increase of normalized tangential traction, friction coefficient and axle load. Among all the three rail steels, the LAHT steel has the best resistance to ratcheting and the longest crack initiation life when the rolling contact condition is mild, i.e. $\xi \leq 0.5$; $f \leq 0.4$; and $L \leq 35$ t. When the rolling contact condition becomes more severe, the LAHT steel has the shortest crack initiation life than the two hypereutectoid rail steels. This reveals that the LAHT steel may not be able to be applied in high traction area of the rail track and support larger axle load in practice. The HE1 steel, which has the carbon content of 1%, shows a low resistance to ratcheting and a short crack initiation life when comparing to the HE2 steel, which has the carbon content of 0.85%. This is due to the relatively low ductility limit of the HE1

steel, which is 68% less than that of the HE2 steel. Among all the three rail steels, the HE2 steel has the most consistent resistance to ratcheting and the most consistent crack initiation life under all considered loading conditions. Therefore, the HE2 steel should be the best one to apply in heavy haul railway among all the three rail steels. Also, it is the most potential one to be applied in track for increasing axle load to fulfil the demanding conditions in railway transport of mineral products in Australia.

Comparison between the numerical predictions and the practical investigations show that the numerical results give a reasonable agreement with the in-service performance of the three rail steels. Therefore, the approach developed here, including the experimental program; the developed cyclic plasticity material model; the method of calibrating material parameters; and the method of estimating crack initiation life, has the capacity to evaluate the ratcheting performance of other pearlitic rail steels under actual wheel–rail cyclic rolling contact conditions. The results can then provide useful information to the railway operator(s) for the development of a reliable and cost-effective rail maintenance strategy for a specific rail track.

Acknowledgements

The present work has been partly funded by an Australian Research Council Linkage Project (LP110100655) with support from Rio Tinto Iron Ore. The computational simulations were carried out at the NCI National Facility in Canberra, Australia, which is supported by the Australian Commonwealth Government.

References

[1] Cannon DF, Edel D-O, Grassie SL, Sawley K. Rail defects: an overview. Fatigue Fract Eng Mater Struct 2003;26:865–87.
[2] Wen Z, Wu L, Li W, Jin X, Zhu M. Three-dimensional elastic–plastic stress analysis of wheel–rail rolling contact. Wear 2011;271:426–36.
[3] Olver AV. The mechanism of rolling contact fatigue: an update. Proc Inst Mech Eng J: J Eng Tribol 2005;219:313–30.
[4] Kapoor A. Wear by plastic ratchetting. Wear 1997;212:119–30.
[5] Kapoor A. A re-evaluation of the life to rupture of ductile metals by cyclic plastic strain. Fatigue Fract Eng Mater Struct 1994;17:201–19.
[6] Tyfour WR, Beynon JH, Kapoor A. Deterioration of rolling contact fatigue life of pearlitic rail due to dry-wet rolling–sliding line contact. Wear 1996;197:255–65.
[7] Su X, Clayton P. Ratchetting strain experiments with a pearlitic steel under rolling/sliding contact. Wear 1997;205:137–43.
[8] Kulkarni SM, Hahn GT, Rubin CA, Bhargava V. Elastoplastic finite element analysis of three-dimensional, pure rolling contact at the shakedown limit. ASME J Appl Mech 1990;57:57–65.
[9] Kulkarni SM, Hahn GT, Rubin CA, Bhargava V. Elasto-plastic finite element analysis of three-dimensional pure rolling contact above the shakedown limit. ASME J Appl Mech 1991;58:347–53.
[10] Kulkarni SM, Hahn GT, Rubin CA, Bhargava V. Elasto-plastic finite element analysis of repeated three-dimensional, elliptical rolling contact with rail wheel properties. ASME J Tribol 1991;113:434–41.
[11] Xu B, Jiang Y. Elastic–plastic finite element analysis of partial slip rolling contact. ASME J Tribol 2002;124:20–6.
[12] Jiang Y, Xu B, Sehitoglu H. Three-dimensional elastic–plastic stress analysis of rolling contact. ASME J Tribol 2002;124:699–708.
[13] Hertz H. Uber die Beruhrung fester elastischer Korper. J Reine Und Angew Math 1882;92:156–71.
[14] Yan W, Fischer D. Applicability of the Hertz contact theory to rail–wheel contact problems. Arch Appl Mech 2000;70:255–68.
[15] Vo KD, Tieu AK, Zhu HT, Kosasih PB. A 3D dynamic model to investigate wheel–rail contact under high and low adhesion. Int J Mech Sci 2014;85:63–75.
[16] Chen YC. The effect of proximity of a free edge in elastic–plastic contact between a wheel and a rail. Proc Inst Mech Eng F: J Rail Rapid Transit 2003;217:189–201.
[17] Ringsberg JW. Life prediction of rolling contact fatigue crack initiation. Int J Fatigue 2001;23:575–86.
[18] Ringsberg JW, Josefson BL. Finite element analyses of rolling contact fatigue crack initiation in railheads. Proc Inst Mech Eng F: J Rail Rapid Transit 2001;215:243–59.
[19] Mandal NK, Chanasekar M. Sub-modelling for the ratchetting failure of insulated rail joints. Int J Mech Sci 2013;75:110–22.
[20] Chaboche JL. Time-independent constitutive theories for cyclic plasticity. Int J Plast 1986;2:149–88.
[21] Chaboche JL. On some modifications of kinematic hardening to improve the description of ratcheting effects. Int J Plast 1991;7:661–78.
[22] Chaboche JL. Modeling of ratchetting: evaluation of various approaches. Eur J Mech A/Solids 1994;13:501–18.
[23] Ohno N, Wang J-D. Kinematic hardening rules with critical state of dynamic recovery, Part I: Formulations and basic features for ratcheting behaviour. Int J Plast 1993;9:375–90.
[24] Ohno N. Constitutive modelling of cyclic plasticity with emphasis on ratchetting. Int J Mech Sci 1998;40(2-3):251–61.
[25] Pun CL, Kan Q, Mutton PJ, Kang G, Yan W. Ratcheting behaviour of high strength rail steels under bi-axial compression-torsion loadings: Experiment and simulation. Int J Fatigue 2014;66:138–54.
[26] Magel EE. Rolling contact fatigue: a comprehensive review. Final report, DOT/FRA/ORD-11/24. USA: Federal Railroad Administration; 2011.
[27] Bannantine JA, Comer JJ, Handrock JL. Fundamentals of metal fatigue analysis. Englewood Cliffs, NJ, USA: Prentice-Hall Inc.; 1990.
[28] Yokobori T, Yamanouchi H, Yamamoto S. Low cycle fatigue of thin-walled hollow cylindrical specimens of mild steel in uni-axial and torsional tests at constant strain amplitude. Int J Fract Mech 1965;1:3–13.
[29] Smith KN, Watson P, Topper TH. A stress-strain function for the fatigue of metals. J Mater 1970;5(4):767–78.
[30] Tyfour WR, Beynon JH. The effect of rolling direction reversal on the wear rate and wear mechanisms of pearlitic rail steel. Tribol Int 1994;27:401–12.
[31] Bandula-Heva T, Dhanasekar M. Failure of discontinuous railhead edges due to plastic strain accumulation. Eng Fail Anal 2014;44:110–24.
[32] AbdelKarim M, Ohno N. Kinematic hardening model suitable for ratcheting with steady-state. Int J Plast 2000;16:225–40.
[33] Armstrong PJ, Frederick CO. A mathematical representation of the multiaxial Bauschinger effect. CEGB report RD/B/N731. Berkely, UK: Berkely Nuclear Laboratories; 1966.
[34] Yan W, Busso EP, O'Dowd NP. A micromechanics investigation of sliding wear in coated components. Proc R Soc Lond A 2000;456:2387–407.
[35] Suresh S. Fatigue of materials. 2nd ed. Cambridge, UK: Cambridge University Press; 2002.
[36] Johnson KL. Contact mechanics. Cambridge, UK: Cambridge Unversity Press; 1985.
[37] Haines DJ, Ollerton E. Contact stress distributions on elliptical contact surfaces subjected to radial and tangential forces. Proc Inst Mech Eng 1963;177:95–114.
[38] Carter FW. On the action of a locomotive driving wheel. Proc R Soc London Ser A: Math Phys Eng Sci 1926;112:151–7.
[39] Kalker JJ. A strip theory for rolling with slip and spin. Proc Koninkl Ned Akad Wetenschap Ser B 1967:10–62.
[40] Kalker JJ. Three-dimensional elastic bodies in rolling contact. Kluwer, The Netherlands: Springer; 1990.
[41] Abaqus analysis user's manual version 6.12, Dasssault systemes Simulia Corp, Providence, RI, USA; 2013.
[42] Hassan T, Kyriakides S. Ratcheting of cyclically hardening and softening materials: I. Uniaxial behavior. Int J Plast 1994;10(2):149–84.
[43] Hassan T, Kyriakides S. Ratcheting of cyclically hardening and softening materials: II. Multiaxial behavior. Int J Plast 1994;10(2):185–212.
[44] Stephens RI, Fatemi A, Stephens RR, Fuchs HO. Metal fatigue in engineering. 2nd ed. New York, NY: John Wiley and Sons; 2001.
[45] Zerbst U, Mädler K, Hintze H. Fracture mechanics in railway applications—an overview. Eng Fract Mech 2005;72:163–94.
[46] D. Szablewski, S. Kalay, J. LoPresti, Development and evaluation of high performance rail steels for heavy haul operations. In: Proceedings of the 2011 International Heavy Haul Association conference, Calgary, Canada, 19–22 June; 2011.
[47] D. Szablewski, D. Gutscher, J. LoPresti, S. Kalay, Effect of heavy axle loads on super premium rail steels and rail joining methods. In: Proceedings of the 10th international heavy haul association conference, New Delhi, India, 4–6 Feb, 43–50, 2013.